Plasma Physics and Controlled
Fusion

Low *n* electromagnetic modes in spherical tokamaks

OPEN ACCESS
IOP Publishing
Plasma Physics and Controlled Fusion
Plasma Phys. Control. Fusion **63** (2021) 075017 (12pp)
https://doi.org/10.1088/1361-6587/ac031b

Low *n* electromagnetic modes in spherical tokamaks

J Chowdhury[1,*] and B F McMillan

CFSA, Department of Physics, University of Warwick, Coventry CV4 7AL, United Kingdom

E-mail: jugalchowdhury5@gmail.com

Received 26 October 2020, revised 4 May 2021
Accepted for publication 19 May 2021
Published 3 June 2021

Abstract

The performance of spherical tokamak reactors depends on plasma β, and an upper limit is set by long-wavelength kinetic ballooning modes (KBMs). We examine how these modes become unstable in spherical-tokamak reactor relevant plasmas, which may contain significant fast-ion pressure. In a series of numerically generated equilibria of increasing β, the KBM becomes unstable at sufficiently high plasma β, and for such cases, it is also significantly unstable even in the long-wavelength limit. The β threshold for the KBMs is similar to the ideal Magnetohydrodynamics (MHD) threshold, and in cases without fast ions, their frequencies are as predicted by diamagnetic-drift stabilised MHD. To isolate and explore the KBMs, simulations are performed where the pressure gradient is entirely due to the density profile, or entirely due to the temperature profile; the resulting KBMs have similar properties in the long-wavelength regime. The introduction of energetic ions restricts the KBMs to longer wavelengths, and reduces the β threshold somewhat; for parameter regimes of current-day devices, this is such long wavelength that a global analysis would become necessary. Mode frequencies in plasmas with a significant fast particle population are seen to be controlled by fast particle precession frequencies.

Keywords: kinetic ballooning mode, spherical reactor, gyrokinetic simulation, microinstability, electromagnetic modes, tokamak

(Some figures may appear in colour only in the online journal)

1. Introduction

Fusion reactor power varies approximately as the square of the plasma pressure, and since the magnetic field strength is limited by engineering constraints, good fusion reactor performance requires high normalised pressure. Also, for an H-mode plasma where increasing power only weakly affects the confinement time, the fusion triple product increases with increasing β. Therefore, the success of fusion reactors depends strongly on achieving plasma β as high as possible. However, Magnetohydrodynamics (MHD) instabilities may limit the maximum achievable β in these machines. In particular, pressure-driven ideal MHD modes are observed to control the steepness of the pressure profiles, in some regimes [1]. These modes may set a hard limit on the plasma β in contrast to the less abrupt confinement deterioration produced by typical drift modes. This effect may be attributed to the long-wavelength nature of MHD modes; mixing-length estimates of transport suggests a very strong transport for typical MHD-ballooning growth rates and wavelengths. Though kinetic effects may modify the nature of this hard limit [2], the overall picture does not change too drastically. The unstable kinetic ballooning modes (KBMs) [3–12] are interchange modes due to bad curvature, and thus closely related to ideal MHD ballooning modes; KBMs and ideal ballooning modes have similar β thresholds and are modelled to generate very strong

[*] Author to whom any correspondence should be addressed.
[1] Present Address: Sikkim University, Sikkim, India

transport in the threshold β regime. Note the contrast with the essentially electrostatic ion-scale and shorter wavelength drift modes such as ion temperature gradient (ITG) modes or trapped electron modes (TEMs), that tend to lead to a softer limit to plasma gradients [13–16].

KBMs have been studied in spherical tokamaks (STs) such as mega amp spherical tokamak (MAST) [17, 18]. Pedestal KBMs [19] are important for edge localized mode (ELM) onset [20–22]; the KBM dominant region was found to widen during the ELM cycle [23] and KBMs can regulate the pressure gradient in the pedestal in this cycle [24]. Unlike these studies, the present analysis focuses on the core of STs. KBMs are also observed in a conventional tokamaks, both in the core and edge. For example, high β hybrid JET discharges are shown to KBM unstable in the core [25]. Similarly in high β scenarios, unstable KBMs are shown to exist in the JET pedestal [24]. Studies carried out for DIII-D [26] and ASDEX [27] plasmas also find pedestal KBMs that play an important role in ELM onset. Low aspect ratio can stabilize KBMs [28].

The present work is a study of the linear properties of the KBMs in the core of reactor-relevant, tight aspect ratio plasmas. These plasmas are typically characterized by high β, and a large fraction of the pressure is provided by the energetic ions. Therefore, the interaction of the core KBM with energetic ions is crucial. The ST core β values can be sufficiently high that even the tails of the bulk ion distributions are super-Alfvénic.

We study the linear stability properties of the KBMs for several sets of parameters relevant to ST reactor equilibrium; in each set, the plasma equilibria β is scanned below and above the ideal MHD stability threshold. Thus the set of parameters are designed to encapsulate the transition from the quasi-electrostatic to the electromagnetic regime. The transition from electrostatic to electromagnetic turbulence near the MHD stability threshold has been previously studied using nonlinear simulation [7, 29, 30]. In general, once there are substantially unstable KBM modes present, simulations tend to find physically implausible levels of heat flux, supporting the existence of a hard β limit. However, in this study, linear computation, which is less computationally intensive is considered; this allows studies of parameter dependence, especially in the long-wavelength regime (which is prohibitive for nonlinear simulation), and to compare mode properties to more basic theory in somewhat different regimes.

To conveniently study the long-wavelength KBM mode properties near the MHD instability threshold we consider cases with monotonic q profiles for which the pressure-gradient driven ballooning modes become strongly unstable. It is important to note here that the advanced scenario designs in ST reactors often choose a reversed shear near the axis to mitigate these instabilities in the core. To self-consistently incorporate the modification to flux-surface shape, the global equilibrium is calculated using a Grad–Shafranov solver (CHEASE) [31–33] for each β value and then local parameters are extracted for gyrokinetic simulations of the core using GENE [34–36]. The main aim of the investigation is to identify the wavelength range where KBMs become unstable and the mode properties. A significant fraction of the plasma pressure is expected to be due to fast particles in an ignited plasma. These fast particles interact with plasma instabilities [37–41]. Here, we examine how this modifies the transition to KBM instability and the mode properties. Qualitatively, one important question is whether the KBMs seen in the local analysis are substantially unstable in the long-wavelength limit, or whether the growth rates are much larger at finite $k_y\rho_i$. The system-scale modes have very different observational features and consequences on overall performance of the reactors. Earlier investigations have shown that this depends strongly on local parameters, with a short pressure gradient scale length leading to a dominance of long-wavelength instability, and we show in this study that plasmas with a large fast particle pressure also tend to become unstable at long wavelength.

Ultimately, this study is designed to feed into transport simulations that determine the transport fluxes in reactors operating at high-beta, but these local simulations also probe parameter regimes relevant to smaller current-day STs like MAST [42]. From these linear simulations, ratios of fluxes may be calculated to allow some insight into the transport expected in the nonlinear saturated transport state. Because the KBMs are likely to imply a hard limit on device β, the higher β configurations we study are probably not realisable; this is mostly an indirect approach to deducing behaviour near the threshold. We also explore the relationship between these KBMs and ideal MHD ballooning modes in certain regimes. The manuscript is organized as follows. Section 2 discusses the equilibria that are used in the simulations. Section 3 discusses the linear results for KBM. Section 4 presents the properties of the KBM in the presence of energetic/fast ions. Section 5 presents estimation of kinetic effects due to fast particles. Finally, results are summarized in section 6.

2. Details of the equilibria

In this section, we discuss the MHD equilibria which will be used for stability studies. This is unlike the procedure most commonly used, which involves scaling the pressure gradient in local simulations by fixing the flux surface shape at a specific minor radius and adjusting the pressure gradient (the Miller *et al* [43] parameters are modified to account for finite β effects). The local fixed-surface-shape approach captures certain important finite-β equilibrium effects on KBMs. One reason for our choice is that we wish to later be able to consider stability across the whole device and make contact with global analysis. Another is that this comes closer to experimentally relevant cases, and ensures that there is a reasonable global MHD equilibrium associated with the local parameters.

We use numerical equilibrium generated by the CHEASE code [31–33]. Figure 1(a) shows the up-down-symmetrical outermost flux surface chosen (this is similar to typical MAST shots). The relative pressure and toroidal current profiles p/c_1^2K and I^*/c_1 chosen are shown in figure 2 (see [32] for the definition of I^*). The equilibria are scaled via the constant c_1 and the transformation $FF' \rightarrow FF' + c_2$ to ensure that $F(0) = 1$ (F is the product of the toroidal field strength and R, so for $R_0 \sim 1$ this implies $B_0 \sim 1$) and fix the volume-averaged

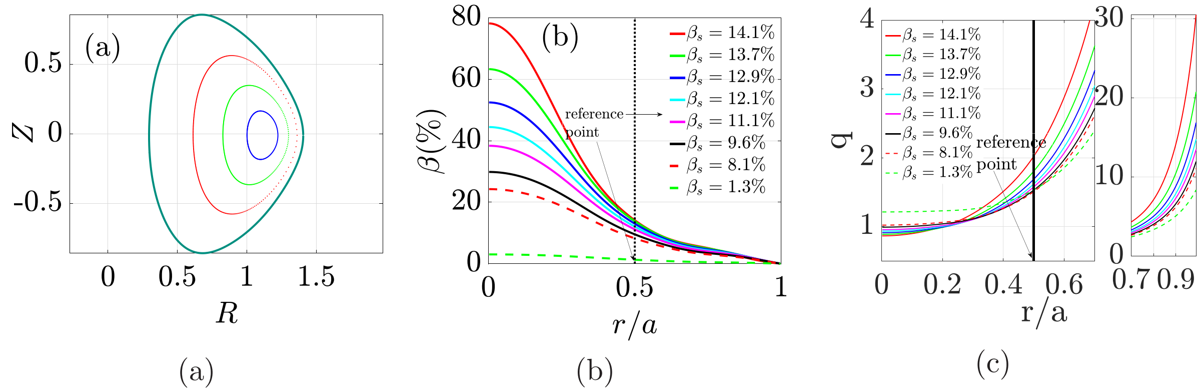

Figure 1. (a) Shape of the last closed flux surface and several inner flux surfaces, with normalised $\psi = 0.72,\ 0.38,\ 0.1$ for $\beta = 12.1\%$ (in arbitrary spatial units). (b) β profiles for the set of equilibria. The values in the legend represent total β values at the location $r/a = 0.5$. (c) q profiles for these cases.

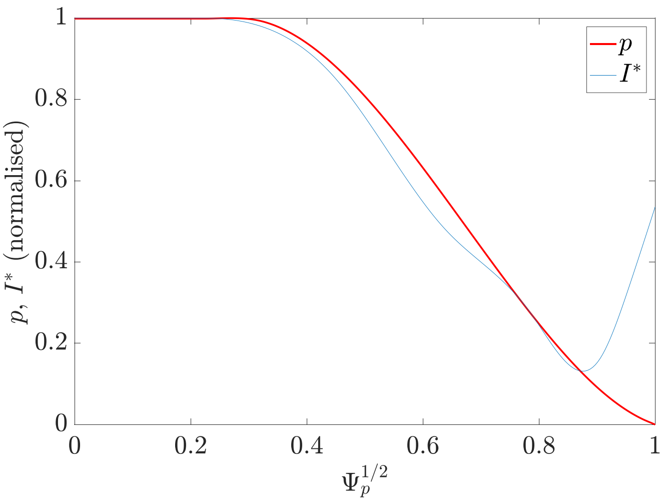

Figure 2. Normalised pressure (p, thick red trace), and toroidal current profiles (I^*, thin blue trace) versus radial parameter $s = \sqrt{\Psi_p}$ for the chosen MHD equilibria (Here, Ψ_p is the normalised poloidal flux, defined to be 0 on axis and 1 at the equilibrium outer boundary).

current. Figure 1(b) shows the eight equilibria of varying $\beta = p/(B^2/2\mu_0)$; this scan is generated by scaling the pressure profile $p(\Psi)$ using the constant K. The values are plotted with respect to r/a; r is the geometrical minor radius of the flux surface (half the geometrical width of the flux surface) and $a = r$ at the outermost flux surface. The equilibria are labelled by the β values at $r/a = 0.5$ which is the location where local gyrokinetic simulations are performed. Figure 1(c) shows the q profiles with respect to r/a for the set of equilibria; although the current density profiles are fixed, q profiles vary somewhat with β, especially for the three highest β cases, and near the edge.

For self-consistency, the pressure gradient scale length and β in gyrokinetic simulations will be chosen consistent with the Grad–Shafranov equilibria, but this does not fix the partition between density and temperature gradients, or amongst the species.

The Shafranov shift plays a crucial role in the stability properties of microinstabilities [11]; it usually has a stabilizing effect on KBM instabilities [8, 24], and is key to achieving second-stability [44]. But for negative shear, the Shafranov shift destabilizes the ballooning mode [45]. Subtle effects of equilibrium representation can be important for correctly resolving KBM growth rates [46].

Miller parameters [43] are found to approximately parameterise the numerical flux surfaces at $r/a = 0.5$, and then used to specify the flux surface geometry in the GENE code (a good fit was confirmed by plotting the Miller and numerical surfaces). The values of the various parameters for these equilibria (at $r/a = 0.5$, except for the last row, which is on-axis) are given in table 1. In the table, q, $\hat{s}$, κ, δ, dR/dr, R/L_p, respectively, are safety factor, magnetic shear, elongation, triangularity, the derivative of the radial coordinate of the centre of the flux surface, and the normalised pressure gradient.

The ideal-MHD ballooning-mode growth rate, in the incompressible limit, for these equilibria is shown in figure 3. The growth rates are obtained by numerically solving the ballooning stability equation of Greene and Chance [47], modified to include plasma inertia effects. To include inertia effects, the ballooning equation (equation (30) in Greene and Chance [47]) $\frac{\partial}{\partial\theta}\alpha(\theta)\frac{\partial}{\partial\theta}\xi - [K(\theta) - \omega^2]\xi = 0$ is replaced by $\frac{\partial}{\partial\theta}\alpha(\theta)\frac{\partial}{\partial\theta}\varepsilon - [K(\theta) - \omega^2\alpha J^2/f^2]\xi = 0$ (for details of notation see Greene and Chance [47]). As might be expected, this shows the strongest growthrates in the high-pressure gradient region of the core and near the edge. Near the core, relatively low-β case are unstable, likely as a result of very weak global shear. At $r/a = 0.5$, the instability is marginally stable for $\beta = 8.1\%$. These stability calculations are performed at ballooning angle $\theta_0 = 0$ (where modes are radially aligned on the midplane), but an additional calculation is shown for the $\beta = 12.1\%$ case at $\theta_0 = 0.4$. The finite ballooning angle has a very strong stabilizing effect at $r \gtrsim 0.4$ and very little for $r \lesssim 0.3$. Little effect near the axis is an expected consequence of the weak magnetic shear there.

3. Linear simulations, two-species cases

This section presents a linear study of unstable modes in a plasma with two species, D ions and electrons, which are

Table 1. Parameters used in GENE simulation at $r/a = 0.5$.

β	1.3%	8.1%	9.6%	11.1%	12.1%	12.9%	13.7%	14.1%
q	1.538	1.508	1.529	1.584	1.624	1.704	1.818	2.031
$\hat{s}$	0.814	1.045	1.106	1.206	1.264	1.360	1.467	1.629
κ	1.306	1.32	1.332	1.354	1.373	1.399	1.440	1.505
δ	0.096	0.114	0.120	0.132	0.141	0.155	0.175	0.208
dR/dr	−0.098	−0.266	−0.300	−0.349	−0.380	−0.420	−0.467	−0.525
R/L_p	5.833	6.369	6.514	6.682	6.811	7.004	7.265	7.678
β(axis)	3.04%	24.26%	29.84%	38.35%	44.44%	52.44%	63.26%	78.13%

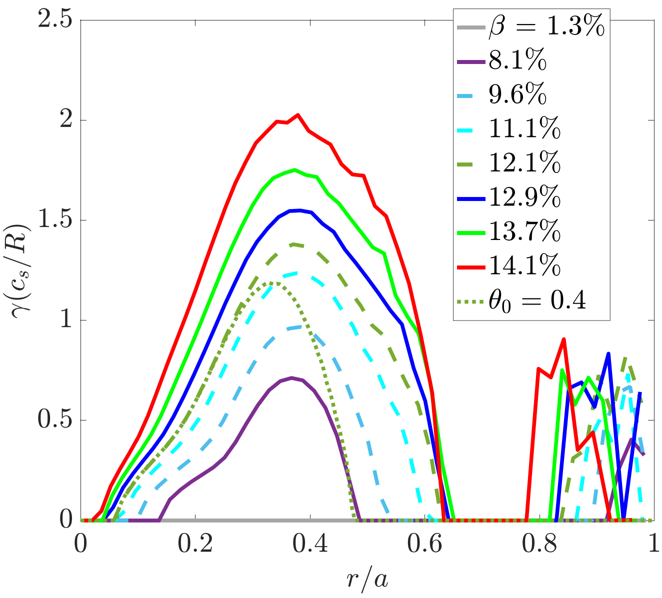

Figure 3. Ideal MHD ballooning mode growth rate versus geometric minor radius r/a. The curves are labelled using the mid-radius β value. Dotted curve is $\beta = 12.1\%$, for ballooning angle $\theta_0 = 0.4$ (all other curves at $\theta_0 = 0$).

locally at the same temperature, in the equilibria described in the previous section. We use the flux tube version of the widely used comprehensive gyrokinetic code GENE [34–36]. The $B_\parallel$ fluctuations are included. But the collisions and equilibrium E_r effects are neglected. To help isolate the KBMs, which are pressure driven modes, cases are first considered with a flat temperature profile, and a density profile consistent with the MHD equilibria as shown in figure 4. Later, a flat density profile is considered, so the pressure gradient arises due to the temperature gradient (this is more reactor-relevant, but supports a wider variety of instabilities, so we present the simpler case first). Unlike most drift modes, the KBM properties should largely be sensitive to the pressure gradient, rather than whether the gradient is in the temperature or density profile. For all the cases considered, we only identify the most unstable eigenmode; the sharp jumps in frequency as parameters vary, indicate that multiple unstable modes may be present.

Only for the lowest β case, and at low k_y, is the real frequency of the instability in the electron diamagnetic direction (figure 4); the frequency increases with larger β. For the lowest β case TEM [48–51] may be a plausible candidate, and we identify the mode as such even at higher β (where mode structure and frequencies vary smoothly with β). At high β, and longer wavelength (low k_y), modes that we identify as KBM are seen (this identification will be justified later). These first arise for the $\beta = 11.1\%$ case. At the highest β, a sharp jump in frequency is seen between these two types of modes. However, at moderate β, there is not a jump in frequency, suggesting a mixed TEM-KBM mode. The shorter wavelength TEM mode is somewhat stabilised as β increases.

For the $\beta = 11.1\%$ case, where KBM instability is first identified, the longest wavelength mode simulated possesses a significant growth rate, about 50% of the peak growth rate, and a simple mixing-length estimate would suggest turbulent fluxes dominated by long wavelength motion. Calculation of $E_\parallel$, for example, for $\beta = 14.1\%$ for $k_y\rho_s \sim 0.05$ or 0.1 shows that $E_\parallel$ is very small, consistent with ideal MHD character. Similar calculations for the lowest β case shows that the inductive component of $E_\parallel$ is very small implying that the mode is largely electrostatic.

Figure 4 also shows a comparison of the real mode frequencies in gyrokinetic theory with diamagnetic-drift stabilised MHD, where the mode frequency scales as $\omega_{pi}/2$ [3, 5] (ω_{pi} is the diamagnetic drift frequency). The KBM frequencies match quite well with this curve (which varies only weakly with β, and is evaluated for the $\beta = 14.1\%$ case). Even though at lower β values there is not a sharp transition from KBM to TEM, at least in the long wavelength limit the dispersion still appears to match this simple theory.

Note that the values of the growth rate in the $k_y \to 0$ limit are also a good match to ideal MHD ballooning theory; for example, the $\beta = 12.1\%$ case has $\gamma \sim 0.9\ c_s/R$ in this limit, whereas the MHD growthrate is 1.1 c_s/R.

We now report linear simulations with a temperature gradient but flat density, which are summarised in figure 5. At the lowest β value, the low k_y modes in the ion diamagnetic direction are identified as ITG, and the higher k_y modes in the electron direction as TEM. For this case, the electrostatic potential of both modes has ballooning parity. At and above $\beta = 11.1\%$, KBMs are observed at long wavelength, with frequencies linearly proportional to k_y. The growth rates of the KBM modes increase with β; these growth rates peak at long wavelength, $k_y\rho_s \sim 0.15$ but the growth rate in the long wavelength limit is not much lower than the peak growth rate,

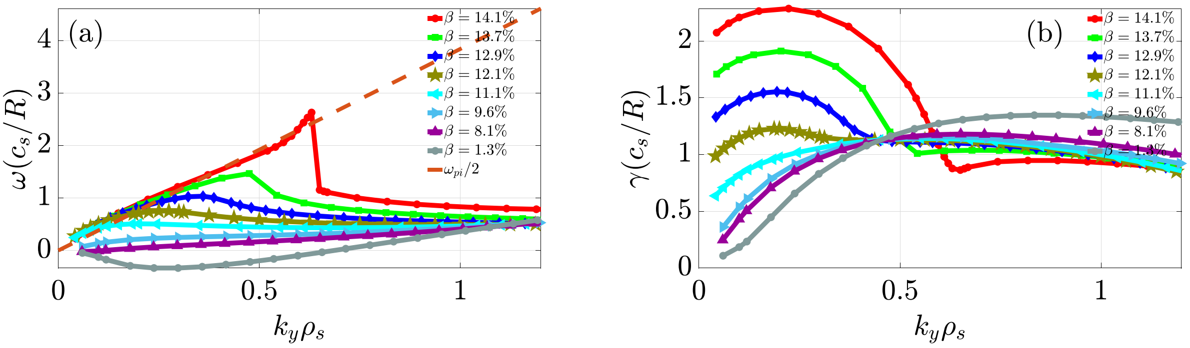

(a) (b)

Figure 4. Real frequencies (a) and growth rates (b) versus $k_y\rho_s$ for the density gradient driven case (temperature flat), for two-species simulations.

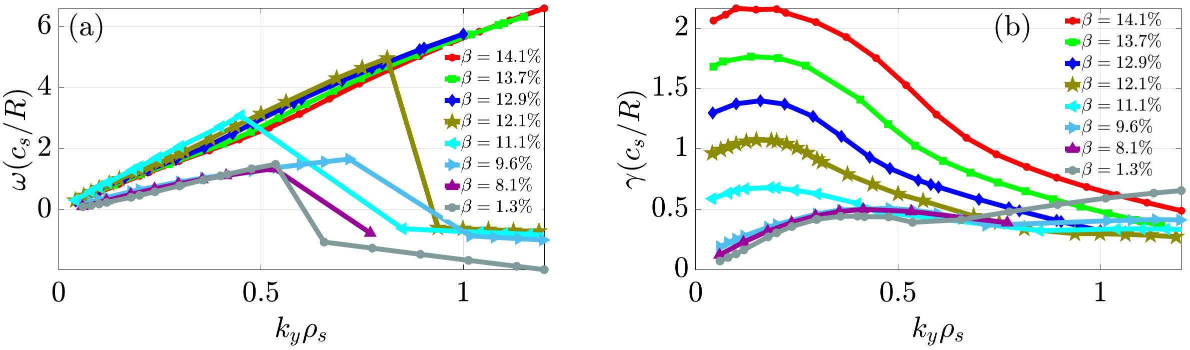

(a) (b)

Figure 5. (a) Real frequency and (b) growth rate of the fastest growing modes, versus $k_y\rho_s$, for temperature gradient driven (flat density) two-species cases.

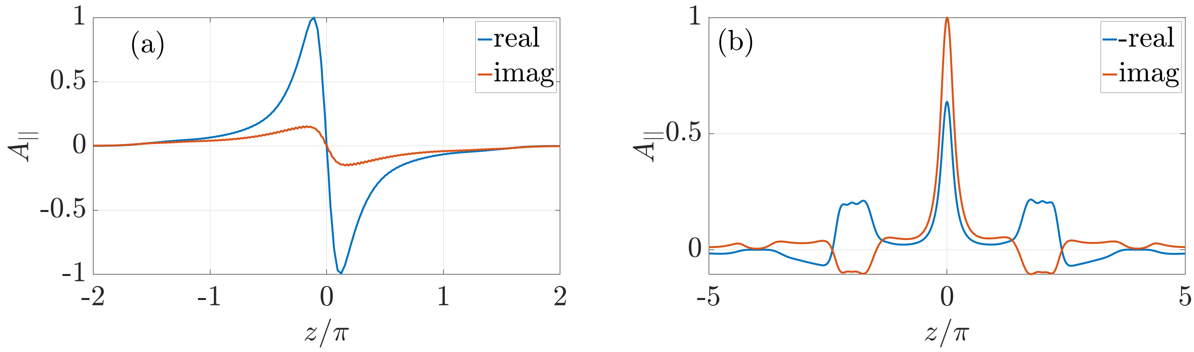

(a) (b)

Figure 6. $A_\parallel$ as a function of z for (a) $k_y\rho_s = 0.414$ and (b) $k_y\rho_s = 0.77$ for $\beta = 8.1\%$.

as in the density-gradient driven case. For all but the lowest β case, the vector potential of the modes in the electron diamagnetic direction exhibit even parity (consistent with tearing modes [52–54]) and are therefore microtearing modes [52, 55–58]. A comparison for $A_\parallel$ in the ballooning space is shown in figure 6 for $\beta = 8.1\%$ and for $k_y\rho_s = 0.414$ and $k_y\rho_s = 0.77$ which exhibit real frequency respectively in the ion and electron direction. $A_\parallel$ for $k_y\rho_s = 0.414$ shows odd parity and for $k_y\rho_s = 0.77$ even parity. More generally the frequencies and growth rates of the modes identified as KBMs (but not the other drift modes) in the temperature gradient driven case are similar to the density gradient driven case, as expected.

We also studied the effect of ballooning angle θ_0 on the growth rates and real frequencies of the KBM for the density gradient driven case and $\beta = 12.1\%$. Figure 7 shows the corresponding results for $kx_{\mathrm{centre}} = 0$ and 0.1. The long

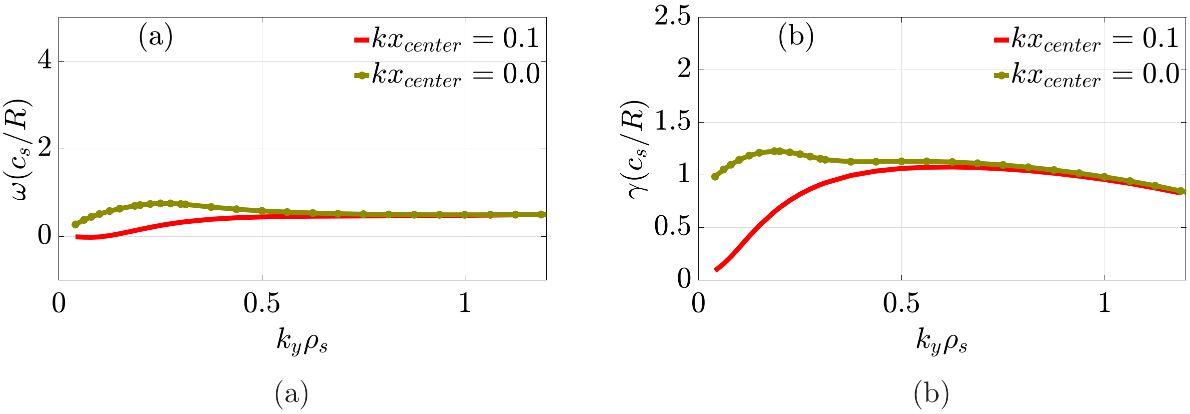

Figure 7. Real frequency (a) and growth rates (b) versus $k_y\rho_s$ for $kx_{\mathrm{centre}} = 0, 0.1$ for density gradient driven KBMs at $\beta = 12.1\%$.

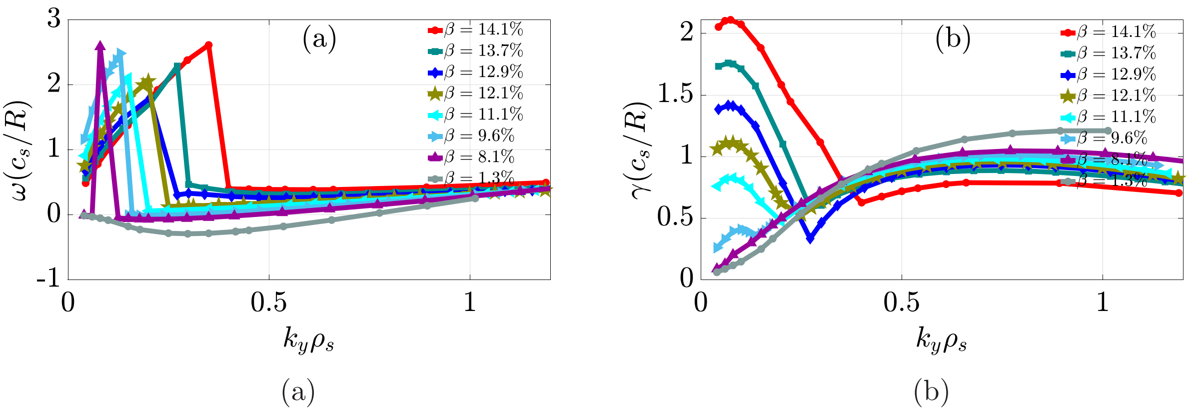

Figure 8. Real frequency (a) and growth rates (b) versus binormal wavenumber of density gradient driven modes in the presence of energetic ions with $\beta_f/\beta = 20\%$.

wavelength KBM branch vanishes away from $\theta_0 = 0$. A kx_{centre} scan for $k_y\rho_s = 0.2$ mode and quadratic fitting to the first few points (not shown here) suggests a stabilisation rule of the form $\gamma = \gamma_0[1-(\theta_0/\theta_k)^2]$, with $\theta_k \sim 0.4$. However, despite the KBM being stabilised at $\theta_k \sim 0.4$, a weaker instability is still present at $k_y\rho_s \lesssim 0.4$, which is determined to be an unstable TEM.

4. Effect of energetic ions

In this section, we investigate the effect of energetic ions, which might arise either due to external heating systems or fusion power, on microinstabilities. The is modelled by adding an additional hot, thermal, D component to the plasma, but since the collisionless physics only depends on the mass-to-charge ratio, the conclusions also apply to He ions with temperature higher by a factor of two and the same pressure. Instabilities, in general, are somewhat sensitive to the shape of the distribution function [59] (energetic ions would usually not be thermal), but for the study of generic tokamaks focused on pressure-driven instabilities, a thermal approximation may suffice.

The baseline temperature ratio chosen for the study is $T_f/T_e = 25$, the density ratio is $n_f/n_e = 0.02$ and the energetic ion β is about 20% of the total plasma β; such levels of fast particle pressure are reached in certain experiments [60] and typical in ST reactor designs [61–63]. In these scans, the background plasma temperature is lowered so the total β stays consistent with the numerical MHD equilibria. That is, the fast particles change the nature of the drive relative to the equivalent case without fast particles, but not its strength. To aid comparison with the zero-fast-particles cases, the fast particle density/pressure profiles are proportional to the background species profiles.

Figure 8 shows the real frequency and growth rates for the density-gradient-only case in the presence of energetic ions. The real frequencies of KBMs in figure 8(a), which appear at long wavelength, are again roughly proportional to wavenumber; but unlike in the two-species case the frequency decreases quite strongly with β. The real frequencies of KBMs are also much higher in the energetic-ion cases and not in agreement with diamagnetic-drift stabilised MHD. We will show that the fast particle pressure is strongly out of phase with the background species pressure; this appears to be largely due to the rapid precession of the trapped fast ions; the tight aspect ratio means that these comprise a substantial fraction of the driving pressure. A dimensional estimate of the fast ion precession frequency may be obtained as

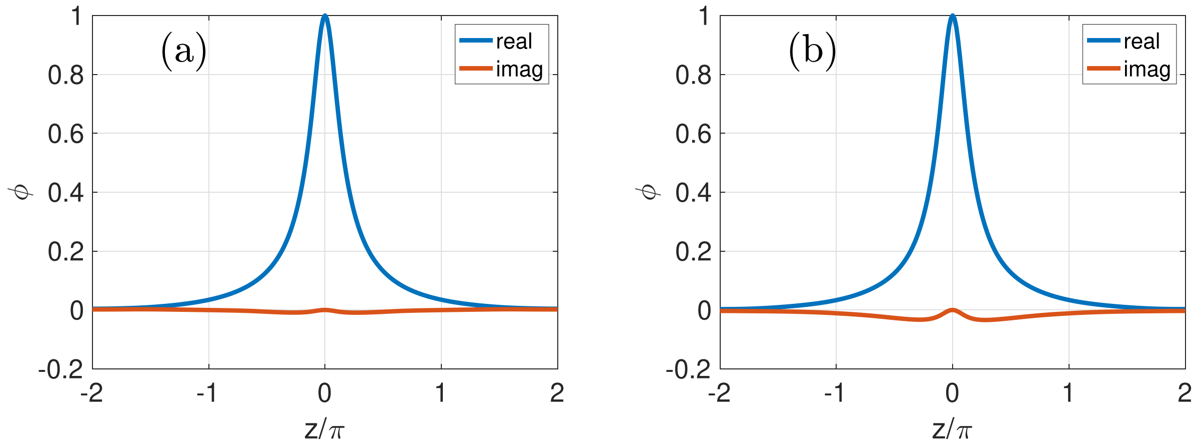

(a) (b)

Figure 9. Electrostatic potential ϕ versus parallel coordinate z for $k_y\rho_s = 0.1$ and $\beta = 12.1\%$ without (a) and with (b) energetic ions.

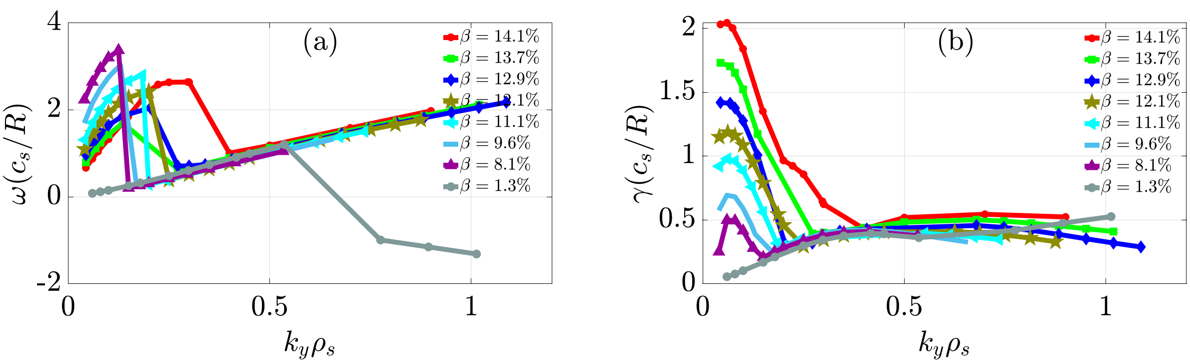

(a) (b)

Figure 10. Real frequency (a) and growth rates (b) versus binormal wavenumber of temperature gradient driven modes in the presence of energetic ions with $\beta_f/\beta = 20\%$.

$$\omega_p = (k_\perp \rho_i)(T_f/T_i)c_s/R \tag{1}$$

but this estimate assumes the magnetic field strength scales as $1/R$, which is increasingly not the case in the higher β simulations. In this case,

$$\omega_p = (k_\perp \rho_i)(T_f/T_i)c_s|\nabla B|/B \tag{2}$$

is a better estimate. The ∇B reversal in the unstable region in the higher β cases thus might be a plausible reason for the decrease in mode frequency with β, because this reduces the net precession frequency of the trapped particles.

The real frequencies of KBMs are also much higher in the energetic-ion cases and not in agreement with diamagnetic-drift stabilised MHD. We will show (in section 5) that the fast particle pressure is strongly out of phase with the background species pressure; this appears to be largely due to the rapid precession of the trapped fast ions; the tight aspect ratio means that these comprise a substantial fraction of the driving pressure. The ∇B reversal in the unstable region in the higher β cases might be a plausible reason for this trend, because this reduces the net precession frequency of the trapped particles.

Unlike in the two-species case, there is a clear k_y value where the long-wavelength KBM becomes subdominant to another kind of mode. As β increases and the real growth rate of the KBMs increases (figure 8), the KBMs are dominant up to higher k_y. In general, unstable KBMs are observed at lower k_y compared to the two-species case, but the equivalent two-species case does not show a sharp transition, so a direct comparison is difficult. Direct FLR effects might explain why the KBMs are not unstable much beyond $k_y\rho_s = 0.2$, where $k_y\rho_f = 1$, but the dephasing of the fast particle and background pressure fluctuations is likely to also play a role. Figure 9 shows the mode structure of ϕ with and without energetic ions for the $\beta = 12.1\%$ density gradient driven case. The mode structures are qualitatively similar in the both cases; ideal MHD would find modes with constant complex phase, so the small imaginary part is indicative of kinetic effects, which are slightly larger for the case with fast ions. This is also the case for $A_{||}$ (not shown here).

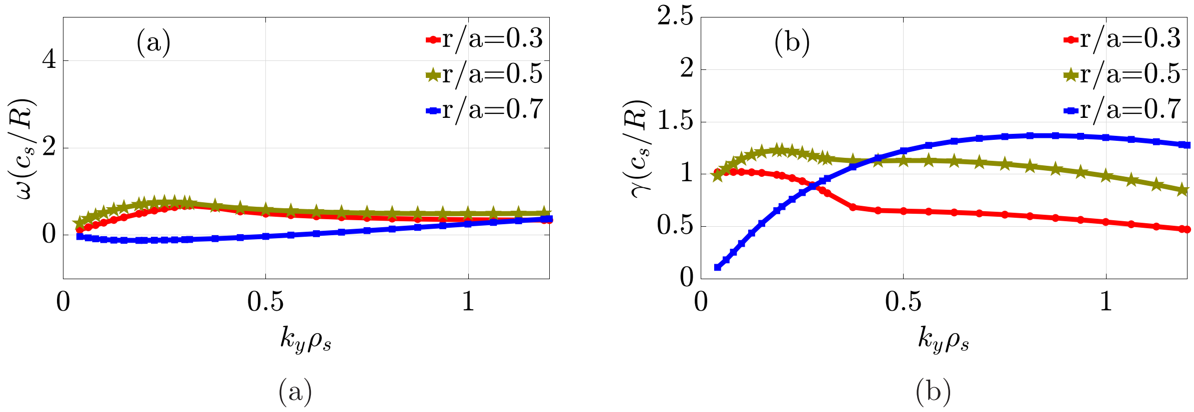

Figure 11. The real frequency (a) and growth rates (b) versus $k_y\rho_s$ for the location $r/a = 0.3,\ 0.5,\ 0.7$ for the two-species case (no fast ions).

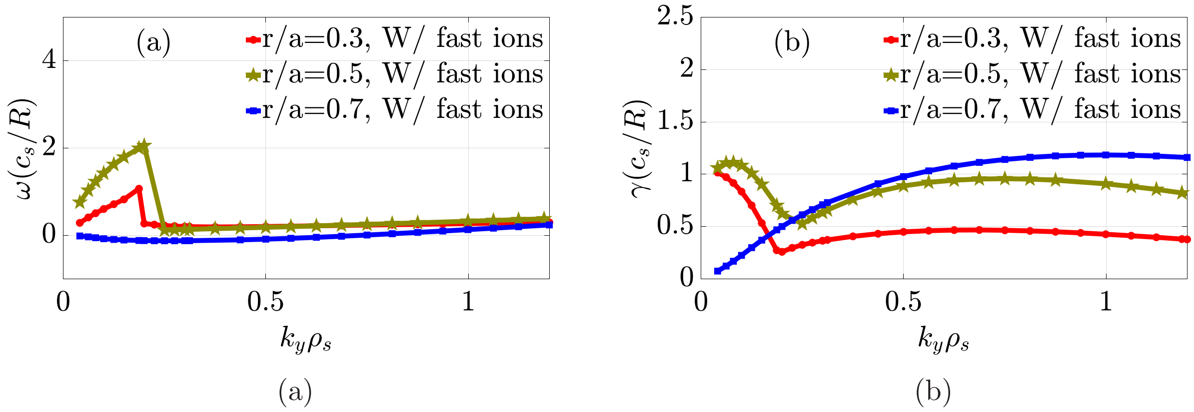

Figure 12. The real frequency (a) and growth rates (b) versus $k_y\rho_s$ for the location $r/a = 0.3,\ 0.5,\ 0.7$ with fast ions.

Figure 10 shows the effect of energetic ions on the real frequencies and growth rates of the KBM for the case with temperature gradients only. The overall qualitative picture remains the same as in the density-gradient driven case. However, in the presence of temperature gradients, there is a wider range of modes that can become unstable and compete with the KBM. Again, generally, the energetic ions destabilise the KBMs more effectively at a long wavelength than in the two-species case, but the KBM becomes subdominant at longer wavelengths in the case with energetic ions.

We carried out simulations for $r/a = 0.3$ and $r/a = 0.7$ for the $\beta = 12.1\%$ (at mid-radius) density gradient driven case and compare with the case for $r/a = 0.5$ of figure 4. We first show the results without energetic ions in figure 11. The KBM mode is unstable at $r/a = 0.3$. However, for $r/a = 0.7$ the KBM mode is stable. This is in conformity with MHD calculations presented in figure 3.

The calculations with energetic ions for the same cases are shown in figure 12. Again the effect of energetic ions for the case at $r/a = 0.3$ is similar to that discussed in the context of figure 8. The location at $r/a = 0.7$ is KBM stable even in the presence of energetic ions. However, this equilibrium does not have representative profiles near the pedestal, so we did not simulate the case at $r/a = 0.9$. Note that the frequencies of the fast particle-driven KBMs at $r/a = 0.3$ are roughly halved compared to the $r/a = 0.5$ case at equal $k_y\rho_s$; this is consistent with the notion that trapped-particle precession is driving the mode frequency, since the trapped particle fraction is considerably smaller at $r/a = 0.3$.

5. Estimating kinetic effects due to fast particles

In the low frequency limit, MHD ballooning theory predicts constant fluid pressure along the field line, so pressure is constant in the frame moving with the fluid, and the perturbed pressure δp can be related to the background pressure p via

$$\frac{\partial}{\partial t}\delta p = -\mathbf{v}\cdot\nabla p \tag{3}$$

where v is the MHD fluid velocity. The phase angle or argument $\mathrm{Arg}(X) = \phi$ is the imaginary part of the logarithm of ϕ, defined such that $X = |X|\exp(i\phi)$. The phase of pressure perturbations relative to velocity is thus $\mathrm{Arg}(p_0/v) = -\mathrm{Arg}(\Gamma)$ (where $\Gamma = \gamma + i\omega$). The dominant MHD fluid velocity is $v_{ExB} = \mathbf{B}\times\nabla\phi/B$ so the phase of the radial component of the velocity relative to the electrostatic potential is $\mathrm{Arg}(v_r/\phi) = -\pi/2$; we then have $\mathrm{Arg}(p_0/\phi) = -\pi/2 - \mathrm{Arg}(\Gamma)$. For a growing MHD mode, with Γ real, the pressure and potential

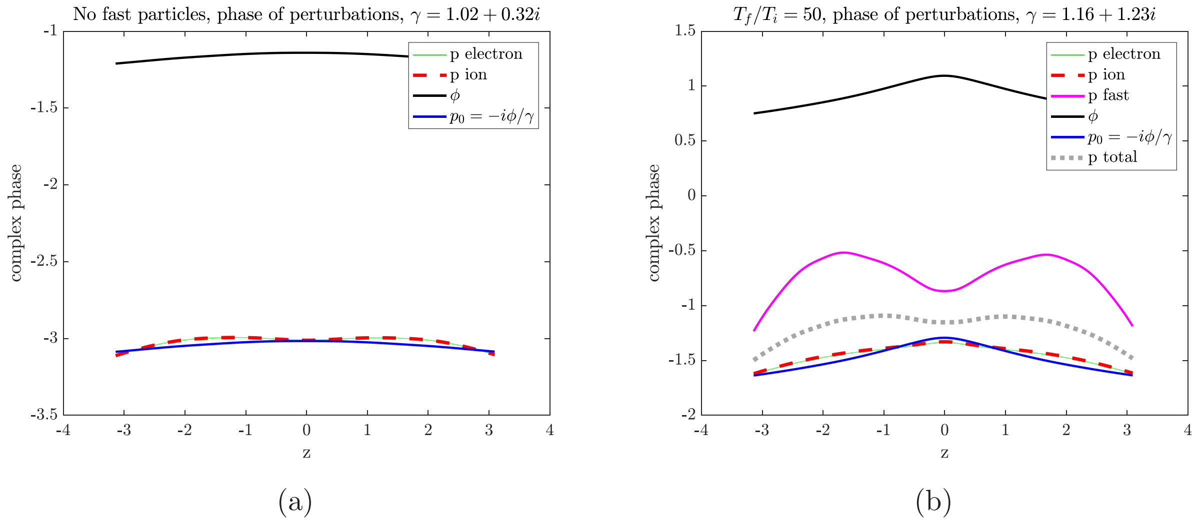

Figure 13. Phases of plasma pressure components (electrons in green trace, ions in red, fast particles pink, total grey), plasma potential (black trace), and fluid model pressure response (blue trace) versus parallel coordinate z for KBM eigenmodes for $k_y\rho_s = 0.05$ without (a) and with (b) fast particles. Note that the ion and electron traces are so similar that they are visually indistinguishable.

are out of phase by $\pi/2$, but this is not necessarily the case when kinetic effects are present.

We evaluate the relative phases of components of the pressure and electrostatic potential in the simulation to explore these kinetic effects (figure 13); the cases examined are density-driven simulations, with $k_y\rho_s = 0.05$, $\beta = 0.121$, with no fast particles, and with $T_f/T_e = 50$ for the case with fast particles. The phase of the fluid and field quantities may be interpreted as an offset in the toroidal angle between the sinusoidal waves in this direction. For the simulation without fast particles, the fluid phase relation is fairly closely reproduced and the predicted phase matches well; also note that in these simulations the pressure fluctuation is almost entirely a density fluctuation, so the ion and electron pressures are constrained by quasineutrality to be near-equal. With fast particles added, the phase relation is still approximately verified by the background ions and electrons, but the fast particles are advanced towards positive phase. The most likely explanation is the fast particle toroidal precession frequency; due to the tight aspect ratio, a large fraction of particles on the outboard side are trapped, and the precession frequencies of the fast particles are larger than those of the bulk species by a factor of the temperature ratio. Direct observation of the phase of the distribution function (not shown) indicates that the trapped particles are indeed advanced in phase. The overall phase of the pressure fluctuation is in between the bulk and fast ion phases.

For this case, the destabilising MHD curvature drive energy κ is a 1.23 times as large as the field line bending term Y (these are the energies associated with these terms, associated with the MHD eigenvector, and found by integrating along the ballooning angle). We consider this as an impact on the total MHD drive

$$\Omega^2_{\mathrm{MHD}} = \kappa - Y \rightarrow \kappa \exp(i\eta) - Y \tag{4}$$

where η is the advance angle of the kinetic pressure response over the MHD model. That is, we are considering the fast particle precession to impact the phase of the MHD curvature drive, and not the amplitude. Because, near marginal stability, κ and Y nearly cancel, this can lead to a small advance angle having a significant effect on mode frequency, and complete stabilisation of the mode for advance angles much less than $\pi/2$.

The ratio between the unmodified and modified squared growthrate in the case with fast particles, using $\eta \sim 0.2$ estimated from figure 13, is $0.9 + 1.06i$. If this estimate is scaled to match the real part of the growthrate, we predict a mode frequency of $0.54\ c_s/R$, which is somewhat below that observed: this is at least partly because we have ignored the diamagnetic effects, which are sufficient to give the zero-fast-ion case a real frequency of $0.32\ c_S/R$.

η is expected to scale roughly with $k_\perp$, and this suggests that the modified growthrate should approach zero at approximately $k_y\rho_s = 0.15$ for this case, which is close to the observed stability threshold. As the growth-rate of the mode increases with β, and the precession effect tends to become less significant as the absolute mode frequency increases, this model would predict a smaller advance angle with higher β, and thus lower frequency. This is consistent with the decrease in KBM mode frequency seen at higher β.

5.1. Fast particle temperature ratio dependence

We investigate the influence of the temperature ratio between the background species and the energetic ions; this is shown in figures 14 and 15 for density and temperature gradient driven cases, respectively. In this case, the fast particle density is kept fixed at 1% of the electron density, so the fraction of pressure in the fast particle species is proportional to the temperature ratio. The real frequencies of KBMs in both the density and temperature gradient driven cases increase with increasing T_f/T_e ratio. At modest temperature ratios (more typical of current day devices than reactors), the modification due to addition of fast particles is significant, but qualitatively the

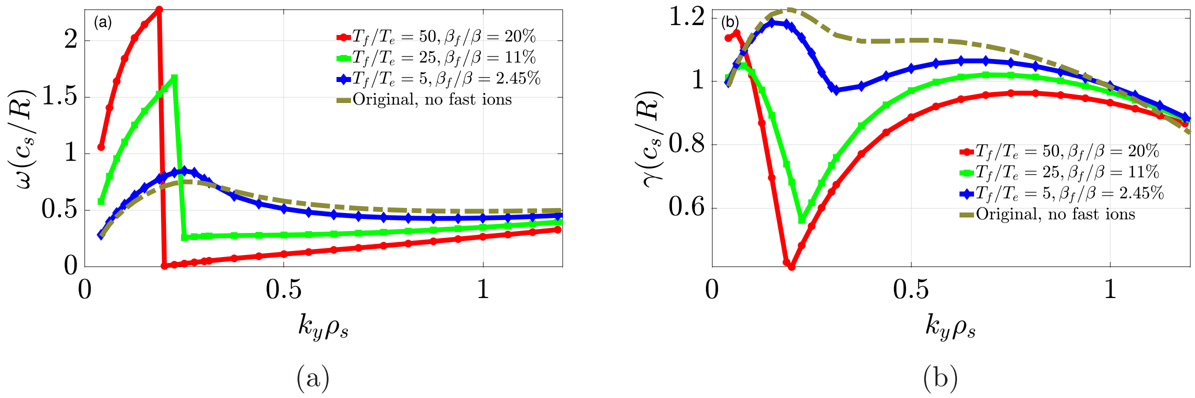

Figure 14. Real frequency (a) and growth rates (b) versus $k_y\rho_s$ for different T_f/T_e for $\beta = 0.121$ for density gradient driven simulations.

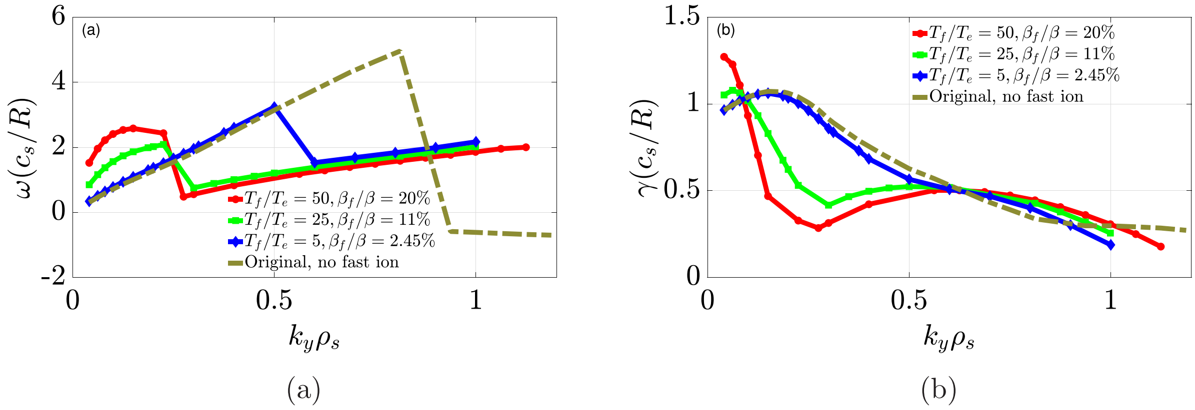

Figure 15. Real frequency (a) and growth rates (b) versus $k_y\rho_s$ for different T_f/T_e for $\beta = 12.1\%$ for temperature gradient driven simulations.

traces look fairly similar. The KBM growth rates at the longest wavelength increase with T_f/T_e, but the wavenumber where the KBMs become subdominant reduces with T_f/T_e. A sharp separation between the KBMs and other modes is seen at sufficiently high T_f/T_e. Note that the frequencies of the KBMs are again proportional to the temperature in this case, consistent with the trapped particle precession-frequency being responsible for setting the frequency. The same trend holds for both density and temperature gradient driven modes in figures 14 and 15.

6. Summary and conclusions

In this work, we examined the linear properties of unstable modes in high β ST reactor-relevant plasmas using numerical MHD equilibria and local gyrokinetic simulations. The focus is on KBMs, which are thought to set a hard β limit, and their relationship to ideal MHD instabilities. Especially in the long-wavelength limit, the KBMs examined here were found to have similar properties and growthrates to ideal MHD ballooning modes. In principle, other kinds of high-β instabilities could have appeared, such as gap modes driven unstable by fast particle resonances, but these were not observed.

We first presented an analysis of two cases without energetic ions (the 'two species' case): one is solely driven by the density gradient and the other is driven solely by the temperature gradient. Although only the temperature-gradient driven case is relevant for instabilities in the tokamak core, the two cases allowed an unambiguous identification of the KBM, which is sensitive mostly to overall pressure gradient (a mixed KBM-TEM is observed in the density gradient driven case though). The KBM frequencies, β threshold, and mode characteristics (e.g. small $E_{||}$, fluid-like transport) are consistent with drift-stabilised MHD theory, demonstrating that these may be seen as modified ideal ballooning modes. Although these have peak growth rate at $k_y\rho_s \sim 0.15$, the KBMs are almost as unstable in the long wavelength limit, suggesting very large transport and a hard β limit. This is in line with results in simpler geometry at large aspect ratio [5], where substantial infinite-wavelength instability is seen given sufficiently strong logarithmic gradients. Given the low mode number of these modes if present in ST devices like MAST, they may be observable directly in magnetic signals.

We also tested the effect of adding an energetic ion species (with a high baseline temperature ratio) with both pure temperature and pure density gradient drive. With energetic ions present, KBMs are excited at lower total β and are only seen at even longer wavelength with wavenumbers $k_y\rho_s \lesssim 0.2$.

This implies that the threshold is reduced with the inclusion of the energetic ions. This is not surprising given the large Larmor radii of the energetic ions, but bounce orbits are also seen to play a significant role. The frequencies of KBMs in the energetic-ion case are controlled by the fast-ions (despite contributing only 20% of the pressure) and we attribute this to trapped particle precession effects; the effect is large because STs have a large trapped particle fraction. Given that these KBMs are able to give rise to transport of all the species, they should be observable through their effects on profiles, and their long wavelength should also facilitate direct external observation. The high energy of the fast particles for the baseline case ($T_f/T_e = 25$) gives rise to a more separate and distinct fast-particle-associated KBM than at lower temperature ratios. The longer wavelengths and higher frequencies are likely to change the nonlinear phenomenology significantly, and may mean these modes are relatively independent from the turbulence at bulk ion scales.

The very long wavelengths of the modes means that a global analysis [64–66] is really needed to understand their influence in (relatively small) existing STs like MAST, where they may give rise to largely-independent eigenmodes, and phenomenology similar to typical fast-particle instabilities, rather than turbulence typical of microinstabilities. For example, at $\rho* = 1/100$, typical of existing STs, toroidal mode number of 1 corresponds to $k_y \sim 0.05$. Similarly, these modes were entirely stabilised at small ballooning angles $k_x/(k_y\hat{s}) \sim 0.4$, which implies a radial mode envelope comparable to the device size in MAST. In current-day STs, fast-ion gyroradii and bounce orbits are large enough that a standard local gyrokinetic treatment of these fast-ions is in any case not appropriate; for example, potato orbits may extend to mid-radius. In larger, reactor-scale devices, fast-ion driven KBMs could potentially set a hard limit on reactor performance more severe than the ideal ballooning threshold, especially if nonlinear effects allow them to be driven below the instability threshold.

STs like MAST often rotate rapidly due to large external torques. Given the narrow peak in ballooning angle of the KBM growth rates these may be strongly suppressed in current day STs (but possibly not reactors with little external torque). We have not included collisions in our simulations, but note that the collisionless KBM growthrates match quite closely the collisional MHD growthrates in the long wavelength limit. Collisions can have a stabilizing effect on KBMs [67] but at least in the pedestal this effect appears weak [68].

Data availability statement

The data that support the findings of this study are available upon reasonable request from the authors.

Acknowledgment

This work was supported by the Engineering and Physical Sciences Research Council (EPSRC) [EP/R034737/1]. This work was supported by the EUROfusion—Theory and Advanced Simulation Coordination (E-TASC). This work has been carried out within the framework of the EUROfusion Consortium and has received funding from the Euratom research and training programme 2014–2018 and 2019–2020 under Grant No. 633053. The views and opinions expressed herein do not necessarily reflect those of the European Commission. Author J C is thankful to Dr T Görler and Dr G Merlo for their help with GENE and CHEASE codes.

ORCID iD

J Chowdhury https://orcid.org/0000-0002-2208-6939

References

[1] Hubbard A E 2000 *Plasma Phys. Control. Fusion* **42** A15
[2] Tang W M *et al* 1985 *Nucl. Fusion* **25** 151
[3] Tang W M *et al* 1980 *Nucl. Fusion* **20** 143
[4] Frieman E A *et al* 1980 *Phys. Fluids* **23** 1750
[5] Aleynikova K and Zocco A 2017 *Phys. Plasmas* **24** 092106
[6] Aleynikova K *et al* 2018 *J. Plasma Phys.* **84** 745840602
[7] Ishizawa A *et al* 2019 *Phys. Plasmas* **26** 082301
[8] Falchetto G L *et al* 2003 *Phys. Plasmas* **10** 1424
[9] Ganesh R *et al* 2004 *Phys. Plasmas* **11** 3106
[10] Ganesh R and Vaclavik J 2005 *Phys. Rev. Lett.* **94** 145002
[11] Belli E A and Candy J 2010 *Phys. Plasmas* **17** 112314
[12] Terry P W *et al* 2015 *Nucl. Fusion* **55** 104011
[13] Horton W 1999 *Rev. Mod. Phys.* **71** 735
[14] Romanelli F 1989 *Phys. Fluids* B **1** 1018
[15] Jagannath M *et al* 2020 *Phys. Plasmas* **27** 052509
[16] Chowdhury J *et al* 2010 *J. Phys.: Conf. Ser.* **208** 012058
[17] Kirk A *et al* 2014 *Nucl. Fusion* **54** 114012
[18] Meyer H *et al* 2013 *Nucl. Fusion* **53** 104008
[19] Wagner F *et al* 1982 *Phys. Rev. Lett.* **49** 1408
[20] Snyder P B *et al* 2002 *Phys. Plasmas* **9** 2037
[21] Wilson H R *et al* 2002 *Phys. Plasmas* **9** 1277
[22] Leonard A W *et al* 2004 *Phys. Plasmas* **21** 090501
[23] Dickinson D *et al* 2011 *Plasma Phys. Control. Fusion* **53** 115010
[24] Saarelma S *et al* 2017 *Plasma Phys. Control. Fusion* **59** 064001
[25] Kumar N *et al* 2021 *Nucl. Fusion* **61** 036005
[26] Holod I *et al* 2015 *Nucl. Fusion* **55** 093020
[27] Hatch D R *et al* 2015 *Nucl. Fusion* **55** 063028
[28] Weening R H 1997 *Phys. Plasmas* **4** 3254
[29] Pueschel M J *et al* 2008 *Phys. Plasmas* **15** 102310
[30] Citrin J *et al* 2015 *Plasma Phys. Control. Fusion* **57** 014032
[31] Luetjens H *et al* 1992 *Comput. Phys. Commun.* **69** 287
[32] Luetjens H *et al* 1996 *Comput. Phys. Commun.* **97** 219
[33] Sauter O and Medvedev S Y 2013 *Comput. Phys. Commun.* **184** 293
[34] Jenko F *et al* 2000 *Phys. Plasmas* **7** 1904
[35] Görler T *et al* 2011 *J. Comput. Phys.* **230** 7053
[36] (available at: http://genecode.org/)
[37] Gorelenkov N N *et al* 2014 *Nucl. Fusion* **54** 125001
[38] Siena A D *et al* 2019 *Phys. Plasmas* **26** 052504
[39] Siena A D *et al* 2018 *Nucl. Fusion* **58** 054002
[40] Wilkie G J *et al* 2018 *Nucl. Fusion* **58** 082024
[41] Chowdhury J *et al* 2012 *Phys. Plasmas* **19** 042503
[42] (available at: https://ccfe.ukaea.uk)
[43] Miller R L *et al* 1998 *Phys. Plasmas* **5** 973
[44] Ma C H and Xu X Q 2017 *Nucl. Fusion* **57** 016002
[45] Elia M and Hirose A 1999 *Can. J. Phys.* **77** 1–83
[46] Xie H S *et al* 2016 *J. Plasma Phys.* **82** 905820503
[47] Greene J M and Chance M S 1981 *Nucl. Fusion* **21** 453
[48] Nordman H *et al* 1990 *Nucl. Fusion* **30** 983

[49] Dannert T and Jenko F 2005 *Phys. Plasmas* **12** 072309
[50] Chowdhury J *et al* 2010 *Phys. Plasmas* **17** 102105
[51] Chowdhury J *et al* 2011 *Phys. Plasmas* **18** 112510
[52] Drake J F and Lee Y C 1977 *Phys. Fluids* **20** 1341
[53] Chen Y *et al* 2015 *Phys. Plasmas* **22** 042111
[54] Chen Y *et al* 2016 *Phys. Plasmas* **23** 056101
[55] Dickinson D *et al* 2013 *Plasma Phys. Control. Fusion* **55** 074006
[56] Swamy A K *et al* 2014 *J. Phys.: Conf. Ser.* **561** 012017
[57] Chowdhury J *et al* 2020 *Phys. Plasmas* **27** 042309
[58] Swamy A K *et al* 2014 *Phys. Plasmas* **21** 082513
[59] Moseev D and Salewski M 2019 *Phys. Plasmas* **26** 020901
[60] McClements K G and Fredrickson E D 2017 *Plasma Phys. Control. Fusion* **59** 053001
[61] Ono M and Kaita R 2015 *Phys. Plasmas* **22** 040501
[62] Menardi J E *et al* 2016 *Nucl. Fusion* **56** 106023
[63] Sykes A *et al* 2018 *Nucl. Fusion* **58** 016039
[64] Collar J P M *et al* 2020 *Plasma Phys. Control. Fusion* **62** 095005
[65] Villard L *et al* 2010 *Plasma Phys. Control. Fusion* **52** 124038
[66] Görler T *et al* 2010 *J. Phys.: Conf. Ser.* **260** 012011
[67] Liu J *et al* 2012 *Nucl. Fusion* **52** 023015
[68] Liao X *et al* 2016 *Phys. Plasmas* **23** 122507